Journal of Rock Mechanics and Geotechnical Engineering 15 (2023) 2917–2929

Contents lists available at ScienceDirect

Journal of Rock Mechanics and Geotechnical Engineering

journal homepage: www.jrmge.cn

Full Length Article

Continuous-discontinuous element method for three-dimensional thermal cracking of rocks

Wen Nie [a], Junlin Wang [a], Chun Feng [b], Yiming Zhang [a,*]

[a] School of Civil and Transportation Engineering, Hebei University of Technology, Tianjin, 300401, China
[b] Institute of Mechanics, Chinese Academy of Sciences, Beijing, 100190, China

ARTICLE INFO

Article history:
Received 14 September 2022
Received in revised form
12 December 2022
Accepted 6 February 2023
Available online 21 March 2023

Keywords:
Rock thermal cracking
Continuous-discontinuous element
Simplex integration
Temperature dependence
Numerical simulation

ABSTRACT

Thermal cracking of rocks can significantly affect the durability of underground structures in engineering practices such as geothermal energy extraction, storage of nuclear waste and tunnelling in freeze–thaw cycle induced areas. It is a scenario of strong coupled thermomechanical process involving discontinuity behaviours of rocks. In this context, a numerical model was proposed to investigate the thermal cracking of rocks, in a framework of the continuous-discontinuous element method (CDEM) for efficiently capturing the initiation and propagation of multiple cracks. A simplex integration strategy was adopted to account for the influences of temperature-dependent material properties. Several benchmark tests were considered and the obtained results were compared with analytical solutions and numerical results from the literature. The results show that the fracture degree of the cases when considering temperature-dependent material parameters had 10% differences approximately compared with the cases with constant parameters.

1. Introduction

Thermal cracking of rocks can occur during shale oil/gas exploration, underground storage of nuclear waste, geothermal energy mining, high geothermal tunnels and constructions in regions with freeze-thaw cycles (Lee et al., 2017; Yuan et al., 2019; Wang et al., 2021; Chen et al., 2022; Luo et al., 2022). Thermal cracking may decrease the safety and durability of geotechnical structures. Many researchers have conducted tests for obtaining the material properties of rocks with varying temperatures. For example, Mao et al. (2015), Fan et al. (2017), and Peng et al. (2020a, b) studied the tensile strength, permeability, fracture morphology and dynamic behaviours of granite. Jiang et al. (2022) studied the influences of high temperature on the changes of mineral composition of granite and green sandstone. Zhang et al. (2017) presented the thermal effects on porous and mechanical parameters of limestone. By using the digital image correlation (DIC), Yang et al. (2022) studied the displacement and strain fields and the crack propagation processes of the sandstone at high temperatures. Li et al. (2021a) used the DIC technique to study the influences of temperature impact on the mechanical properties and fracture behaviours of granite. Junique et al. (2021) proposed the evolution of micro-cracking of cyclic heated granite with infrared thermography. Chen et al. (2017) studied the effects of high temperature on Beishan granite using the acoustic emission (AE) technique and scanning electron microscope (SEM) and they provided the relationship between AE counts and permeability of heated granite. Zhang et al. (2016) tried to understand the effects of water escape process on mineral composition and structure and concluded that the mechanical strength of rocks decreases with increasing temperature. Wang and Konietzky (2019) and Wang et al. (2019a, 2020) suggested the temperature-dependent granite parameters and proposed empirical relations of granite material parameters and temperature. These above-mentioned works reveal the influences of temperature on physical properties of rock materials.

Compared with testing studies, numerical simulations are economically advantageous for large-scale geotechnical structures. Although it is still a challenge for conventional finite element method (FEM) to consider the cracking processes of rock-like materials, many numerical methods, such as the cracking element method (Zhang et al., 2015, 2021a; Zhang and Zhuang, 2018, 2019; Mu and Zhang, 2020; Zhang and Mang, 2020), cracking particle method (Rabczuk and Belytschko, 2004, 2005, 2007; Rabczuk et al.,

* Corresponding author.
E-mail address: Yiming.Zhang@hebut.edu.cn (Y. Zhang).
Peer review under responsibility of Institute of Rock and Soil Mechanics, Chinese Academy of Sciences.

https://doi.org/10.1016/j.jrmge.2023.02.017

2007; Rabczuk and Zi, 2007) and peridynamics (Ren et al., 2016, 2017; Wang et al., 2019b; Shou and Zhou, 2020; Yu et al., 2020; Yu and Sun, 2021; Zhang et al., 2021b), have been proposed to capture the initiation and propagation of multiple cracks in quasi-brittle materials. Tao et al. (2020) adopted a coupled finite element mesh-free method to simulate the thermal cracking processes of rocks. Wu et al. (2021) proposed an extended finite element method based on cohesive zone model to investigate the mixed mode fracture of heated rocks. A TOUGH-RFPA simulator was developed to capture the evolution of thermal stress and damage of heated heterogeneous rocks by Li et al. (2021b). Some methods based on discontinuous medium theory, such as particle and block discrete element model, were also proposed (e.g. Wanne and Young, 2008; Jiao et al., 2015; Xia, 2015; Wu et al., 2019; Wang and Konietzky, 2022). Different from other quasi-brittle materials, there are a large number of faults, joints and mineral particles in rocks where the propagating cracks interact with natural cracks. Distributions of discontinuities can significantly affect the mechanical properties of rocks. Some discontinuity modelling schemes such as discrete fracture network (DFN), discontinuity geometrical modeling (DGM) have been developed (e.g. Boon et al., 2012; Azarafza et al., 2017, 2018; Shang et al., 2018; Rasmussen, 2020; Li et al., 2022).

Continuous-discontinuous element method (CDEM) is a numerical approach combining finite and discrete elements, which is designed to capture this progressive failure process of rocks. The influences of artificial parameters of CDEM such as offset coefficients of semi-spring and semi-edge model, and heat transmission stiffness on the calculation results were studied (Feng et al., 2014; Li and Feng, 2016). Recently, CDEM has been modified and used to simulate hydraulic fracturing, blasting, landslide and other engineering applications (Feng et al., 2014; Ju et al., 2016; Wang et al., 2022), its application to thermal cracking of rocks is still rare (Li and Feng, 2016). Compared with conventional discrete elements, CDEM uses deformable blocks, providing stress/strain results of the domain. Table 1 shows the comparisons of discrete element methods with deformable blocks for thermo-mechanical problems.

In the framework of CDEM, this paper tried to build a three-dimensional (3D) numerical model to study thermal cracking of rocks. The main features of our model include:

Table 1
Comparisons of discrete element methods with deformable blocks for thermo-mechanical problems.

Numerical methods	Computational scheme	Scope	Source
Numerical manifold method	Implicit	Two-dimensional (2D)	Zhang et al. (2014), (2018); Liu et al. (2019)
Extended finite element method	Implicit	2D/3D	Zeng et al. (2020); Chadaram and Yadav (2021); Zhou et al. (2021)
Discontinuous deformation analysis method	Implicit	2D	Zhang (2001); Jiao et al. (2015); Xu et al. (2019); Huang et al. (2022)
Combined finite discrete element method	Explicit	2D/3D	Yan and Zheng (2017); Yan et al. (2021), 2022
Continuous-discontinuous element method	Explicit	2D/3D	Feng et al. (2014); Li and Feng (2016); Ju et al. (2016); Wang et al. (2022)

(i) The temperature-dependent material properties were considered in the framework of CDEM and an updated procedure was established.
(ii) Simplex integration strategy was implemented in the explicit iterative procedure for assuring accuracy.

2. Mathematical model

2.1. CDEM algorithms

The CDEM is an explicit iterative numerical method coupling finite and discrete elements based on the Lagrange function (see Eq. (1)) which can simulate the progressive failure processes of geological bodies from continuous to discontinuous stages (Li and Feng, 2016):

$$\frac{\mathrm{d}}{\mathrm{d}t}\left(\frac{\partial L}{\partial \dot{u}_i}\right)-\frac{\partial L}{\partial u_i}=Q_i \tag{1}$$

where t is the time; Q_i is the non-conservative force of the system; L is the Lagrange function; u_i is the displacement of a node; and $\dot{u}_i$ is the node velocity.

In the CDEM framework, there are two types of basic elements: block and interface. A block contains one or several deformable finite elements, and an interface that contains multiple normal and tangential springs. Finite element method was adopted inside the block elements and discrete element method was used between the blocks when cracks appeared. By implementing corresponding constitutive relations, the tensile-and-shear failure of rocks can be captured (Zhu et al., 2021). In this work, a linear elastic constitutive was adopted for blocks, and the balance equation is

$$\boldsymbol{M}\ddot{\boldsymbol{u}}(t)+\boldsymbol{C}\dot{\boldsymbol{u}}(t)+\boldsymbol{K}\boldsymbol{u}(t)=\boldsymbol{F}(t) \tag{2}$$

where $\boldsymbol{M}$, $\boldsymbol{C}$ and $\boldsymbol{K}$ are the concentrated mass, damping and stiffness matrices of element, respectively; $\ddot{\boldsymbol{u}}(t)$, $\dot{\boldsymbol{u}}(t)$ and $\boldsymbol{u}(t)$ are the acceleration, velocity and displacement vectors of element nodes at time t, respectively; $\boldsymbol{F}(t)$ is the external force vector.

Global dynamic relaxation technique was adopted to solve the displacement and stresses of each block element in the CDEM algorithms. This method introduces a damping term in the dynamic calculation, which makes the initially unbalanced system converge to the equilibrium position gradually.

Brittle fracture Mohr-Coulomb constitutive was used for the interfaces. The displacement increment method was used to calculate the normal and tangential stresses of the contact spring at present time step t_n. In the 3D condition, the force of the contact spring in interface element is written as

$$\left.\begin{aligned} F_{\mathrm{n}}(t_n) &= F_{\mathrm{n}}(t_{n-1})+K_{\mathrm{n}}A_{\mathrm{c}}(-\Delta d_{\mathrm{n}}) \\ F_{\tau 1}(t_n) &= F_{\tau 1}(t_{n-1})+K_{\tau}A_{\mathrm{c}}(-\Delta d_{\tau 1}) \\ F_{\tau 2}(t_n) &= F_{\tau 2}(t_{n-1})+K_{\tau}A_{\mathrm{c}}(-\Delta d_{\tau 2}) \end{aligned}\right\} \tag{3}$$

where F_{n}, $F_{\tau 1}$ and $F_{\tau 2}$ are the normal and two tangential forces of the contact springs, respectively; K_{n} and K_{τ} are the normal and tangential stiffness of the contact springs; A_{c} is the contact area of the springs; Δd_{n}, $\Delta d_{\tau 1}$ and $\Delta d_{\tau 2}$ are the normal and two tangential displacement increments of the contact springs at time t_n, respectively. The negative sign indicates that the displacement is in the opposite direction of the force.

The maximum tensile stress criterion and Mohr–Coulomb criterion were adopted for tensile and shear failures. When the strength is temperature-dependent, it is necessary to judge

whether the spring is broken or not based on the parameter values at current time step. Tensile failure will occur when

$$-F_{\mathrm{n}}(t_n) > A_{\mathrm{c}} f_{\mathrm{t},t_n} \tag{4}$$

where f_{t,t_n} is the tensile strength of spring at time t_n. Shear failure will occur when

$$F_\tau(t_n) > F_{\mathrm{n}}(t_n)\tan\phi + A_{\mathrm{c}} c_{t_n} \tag{5a}$$

$$F_\tau(t_n) = \sqrt{{F_{\tau 1}}^2(t_n) + {F_{\tau 2}}^2(t_n)} \tag{5b}$$

where $F_\tau(t_n)$ is the resultant shear force of spring at time t_n, ϕ is the internal friction angle, c_{t_n} is the cohesion of material at time t_n. All material parameters were updated with varying temperature in the calculation steps.

2.2. Exact integration of heat transfer

Finite volume method was used to capture the heat transfer process in blocks. According to Fourier's law, the heat flux in block element is

$$q_i = -k_{t_n}\left(\frac{\partial T}{\partial x}\vec{i} + \frac{\partial T}{\partial y}\vec{j} + \frac{\partial T}{\partial z}\vec{k}\right) \tag{6}$$

where k_{t_n} is the thermal conductivity of material at time t_n; T is the temperature function; x, y and z are the components of spatial coordinate; $\vec{i}$, $\vec{j}$ and $\vec{k}$ are the direction vectors.

Integrating Eq. (6) in domain Ω, we obtain

$$\boldsymbol{q}_i V = -k_{t_n}\oint_{\partial\Omega}\left(\frac{\partial T}{\partial x}\vec{i} + \frac{\partial T}{\partial y}\vec{j} + \frac{\partial T}{\partial z}\vec{k}\right)\boldsymbol{n}\mathrm{d}s \tag{7}$$

where V is the volume of Ω; $\partial\Omega$ is the boundary of Ω; $\boldsymbol{n}$ is the outer normal vector of $\partial\Omega$; ds is the surface integral of outer surface. In this work, only tetrahedral discretization is considered for Ω (see Fig. 1).

As an exact integration method for polyhedron body (Lin and Xie, 2020), the simplex integration was used to accurately calculate Eq. (7). The temperature of any point in the element shown in Fig. 1a can be determined by

$$\left.\begin{aligned} T(x,y,z) &= \sum_{i=1}^{4} N_i T_i \\ N_i &= \frac{a_i + b_i x + c_i y + d_i z}{6V}\ (i = 1,2,3,4) \end{aligned}\right\} \tag{8}$$

where N_i is the shape function of elements; T_i is the temperature of nodes; a_i, b_i, c_i and d_i are parameters of the shape function (Rao, 2018). Eq. (8) can be transformed into

$$T(x,y,z) = \frac{1}{6V}(A + Bx + Cy + Dz) \tag{9}$$

where $A = \sum_{i=1}^{4} a_i T_i$, $B = \sum_{i=1}^{4} b_i T_i$, $C = \sum_{i=1}^{4} c_i T_i$, $D = \sum_{i=1}^{4} d_i T_i$.

Then, one surface of Ω shown in Fig. 1b is considered as example, denoted as S_{123}, and the plane equation is

$$\alpha(x - x_1) + \beta(y - y_1) + \gamma(z - z_1) = 0 \tag{10}$$

where $\alpha = \begin{vmatrix} 1 & y_1 & z_1 \\ 1 & y_2 & z_2 \\ 1 & y_3 & z_3 \end{vmatrix}$, $\beta = \begin{vmatrix} 1 & z_1 & x_1 \\ 1 & z_2 & x_2 \\ 1 & z_3 & x_3 \end{vmatrix}$, $\gamma = \begin{vmatrix} 1 & x_1 & y_1 \\ 1 & x_2 & y_2 \\ 1 & x_3 & y_3 \end{vmatrix}$.

The total heat flow through S_{123} denoted as q_{123} can be further decomposed into three parts considering its projections on *xoy*, *yoz*, and *xoz* planes (Fig. 2) as

$$\begin{aligned} q_{123} = \iint_{S_{123}} & T(x,y,z)\vec{T_z}\mathrm{d}x\mathrm{d}y + T(x,y,z)\vec{T_x}\mathrm{d}y\mathrm{d}z \\ & + T(x,y,z)\vec{T_y}\mathrm{d}x\mathrm{d}z \end{aligned} \tag{11}$$

where $\vec{T_x}$, $\vec{T_y}$ and $\vec{T_z}$ are the components of the unit normal vectors of the temperature function along the x, y, and z directions respectively as

$$\vec{T_x} = \frac{\alpha}{l}, \vec{T_y} = \frac{\beta}{l}, \vec{T_z} = \frac{\gamma}{l} \tag{12}$$

where $l = \sqrt{\alpha^2 + \beta^2 + \gamma^2}$.

Then we have the following equations

$$q_{123} = q_{123,\,xoy} + q_{123,\,yoz} + q_{123,\,xoz} \tag{13a}$$

where

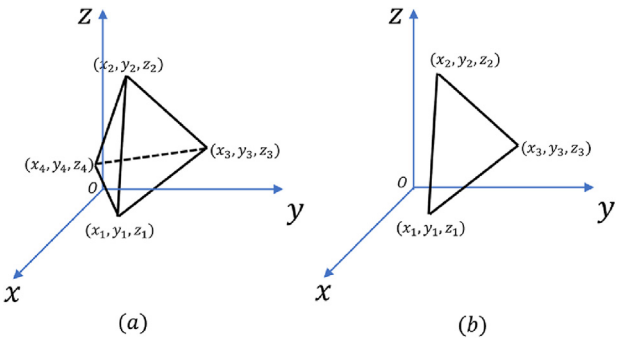

Fig. 1. Tetrahedral element used in this work: (a) one tetrahedral element, and (b) one surface of the tetrahedral element S_{123}.

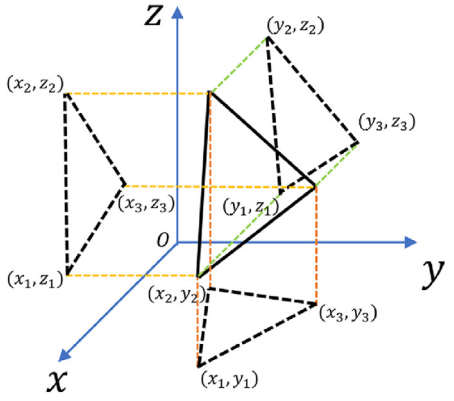

Fig. 2. Projections of S_{123} on *xoy*, *yoz*, and *xoz* planes.

$$\left.\begin{aligned} q_{123,\ xoy} &= \frac{1}{l}\int\int \gamma(A+Bx+Cy)+D[\gamma z_1-\alpha(x-x_1)-\beta(y-y_1)]\mathrm{d}x\mathrm{d}y \\ q_{123,\ yoz} &= \frac{1}{l}\int\int \alpha(A+Cy+Dz)+B[\alpha x_1-\gamma(z-z_1)-\beta(y-y_1)]\mathrm{d}y\mathrm{d}z \\ q_{123,\ xoz} &= \frac{1}{l}\int\int \beta(A+Bx+Dz)+C[\beta y_1-\alpha(x-x_1)-\gamma(z-z_1)]\mathrm{d}x\mathrm{d}z \end{aligned}\right\} \tag{13b}$$

Based on the simplex integration formula in two-dimensional condition (Lin and Xie, 2020), Eq. (13b) can be calculated by linearly superimposing each term. After conducting integrations on all surfaces of Ω, the total energy can be obtained. Then the temperature on the nodes can be updated with

$$\left.\begin{aligned} \Delta T &= \frac{Q_n \Delta t}{c_{\mathrm{p},tn}\rho_{t_n} V} \\ T(t_n) &= T(t_{n-1}) + \Delta T \end{aligned}\right\} \tag{14}$$

where Q_n is the total heat flow of node; Δt is the time increment; c_{p,t_n} and ρ_{t_n} are the specific heat capacity and density of material at time t_n, respectively.

The calculation procedure of CDEM is as follows.

(i) Calculate the temperature increment of block elements according to Eq. (14);
(ii) Calculate the stress of block elements and force of contact springs; and
(iii) Judge whether the spring is broken or not based on the Eqs. (4) and (5).

2.3. Temperature dependent parameters

As mentioned before, the temperature-dependent material parameters were updated in iteration steps. The relations were built based on the formulas in Appendix A (Wang et al., 2020). The mechanical properties such as the Young's modulus, Poisson's ratio, tensile strength, and cohesion are stored in blocks, while thermal parameters such as specific heat capacity and thermal conductivity are stored in nodes. The updating procedure is as follows.

(i) Cycle all block elements and obtain the temperature of each node in each block at current step after solving the temperature field at time t_n;
(ii) Update the thermal parameters on nodes based on the temperature values at time t_n and take the average temperature of all nodes as the temperature of the block; and
(iii) Update the mechanical parameters based on the temperature of the block, and then solve the temperature and stress field at time t_{n+1} (see Fig. 3).

Moreover, the strength reduction induced by elevated temperature is irreversible. In other words, the strength depends on the historical experienced maximum temperature.

2.4. Benchmarks

In this section, three benchmark tests were considered where the obtained results were compared with theoretical solutions and numerical results from the literature.

2.4.1. One-dimensional (1D) heat conduction problem

To validate the numerical results, a model with sizes of 1 m × 0.25 m × 0.25 m (length × width × height) was used. The boundary conditions are $T_{x=0\ \mathrm{m}} = 0\ ^\circ\mathrm{C}$ and $T_{x=1\ \mathrm{m}} = 100\ ^\circ\mathrm{C}$. All points were set to $T_{t=0\ \mathrm{s}} = 0\ ^\circ\mathrm{C}$ as the initial condition. This 1D heat conduction problem was solved by 3D analysis with mesh shown in Fig. 4. The used parameters are density $\rho = 2604\ \mathrm{kg/m^3}$, thermal conductivity $k_0 = 3.65\ \mathrm{W/(m\,^\circ C)}$, specific heat $c_{\mathrm{p},0} = 706\ \mathrm{J/(kg\,^\circ C)}$.

Transient temperature analysis was considered. We simulated the cases with and without temperature-dependent parameters and denoted them as TD (temperature-dependent) and NTD (not temperature-dependent), respectively. The numerical results are shown in Fig. 5. The results indicate that the proposed numerical method can successfully capture the temperature evolution.

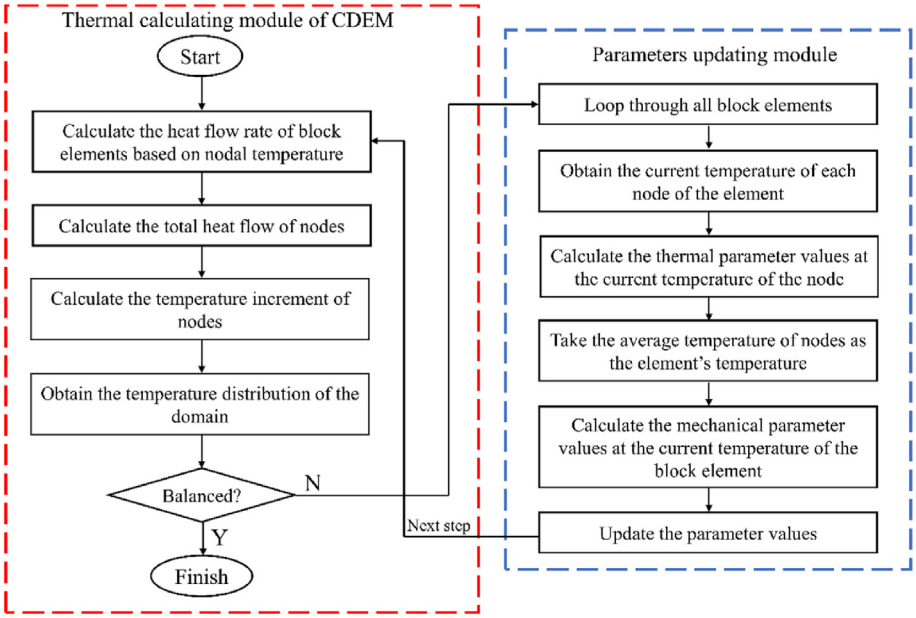

Fig. 3. Flowchart of parameters updating.

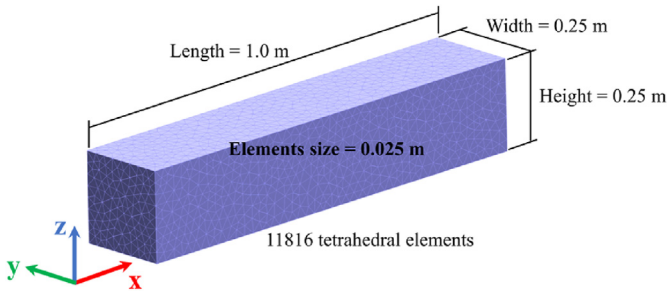

Fig. 4. 1D heat conduction model calculating with 3D analysis.

2.4.2. The disk test

The second example is the disk test with outer radius 1 m and inner radius 0.1 m. Two meshes were considered (Fig. 6). The temperature at outside boundary T_r was set to 0 °C and inside boundary T_R was set to 200 °C. All points were set to $T_{t=0\,s} = 0$ °C as the initial condition. The thermal parameters are the same as those used the last example. The mechanical parameters are the Young's modulus $E_0 = 27.38$ GPa, the Poisson's ratio $\nu_0 = 0.26$, and the thermal expansion coefficient $\alpha_T = 1.482 \times 10^{-5}$ °C^{-1}.

Considering different meshes and NTD condition, the numerically obtained radial and transverse stresses σ_r and σ_θ are shown in Fig. 7 compared with the analytical solutions. The comparisons indicate both meshes can provide agreeable results where finer mesh leads to improved results. Fig. 8 shows the results of TD and NTD conditions. It can be found that the temperature-dependence has slight influences on this example where the difference of σ_r is larger than that of σ_θ.

2.4.3. Thermal cracking of a hollow sphere

A hollow sphere with outer radius 0.1 m and inner radius 0.04 m was considered to study the 3D thermal cracking (Fig. 9). The material parameters are the same as that used in the Sections 2.4.2 and 2.4.3. Additional parameters are the tensile strength $f_{t,0} = 5$ MPa, cohesion $c_0 = 25.5$ MPa and internal friction angle $\phi = 30°$. The initial temperature of model was set as 0 °C. The inner and outer boundaries were set as 100 °C and 0 °C, respectively.

Upon the temperature gradient, the inner part of the sphere experiences compression while the outside part experiences tension. The damage of the model can be quantified by the spring

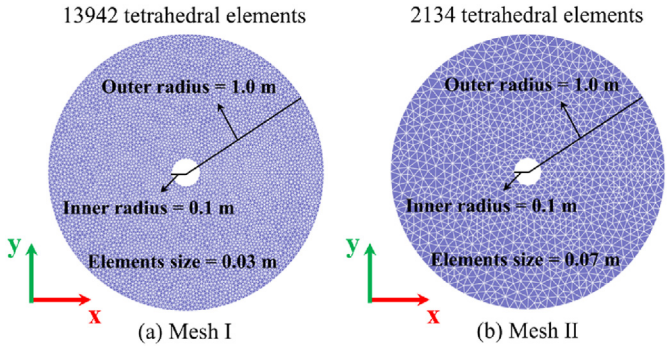

Fig. 6. The disk test.

broken ratio (SBR) as the ratio of the area of broken springs to the area of total springs (see Fig. 10). After applying the boundary, the thermal cracking happens from 1000 s to 3000 s. For the TD condition, the obtained SBR is lower than that of the NTD condition. The cracking patterns are illustrated in Fig. 11 where the cracks emerge from the outer to the inner regions. The cracking patterns agree with the results of Yan et al. (2021).

3. Numerical examples

3.1. Thermal shock of a heated block

The thermal shock of a heated block (Yan et al., 2022) was simulated in this section. The plate has the dimensions of 0.15 m × 0.15 m × 0.05 m (length × width × height) (Fig. 12). The material parameters are $\rho = 3900$ kg/m^3, $E_0 = 300$ GPa, $\nu_0 = 0.3$, $k_0 = 30$ W/(m °C), $c_{p,0} = 880$ J/(kg °C), $\alpha_T = 7.5 \times 10^{-6}$ °C^{-1}, $f_{t,0} = 180$ MPa, $c_0 = 200$ MPa and $\phi = 30°$. The initial temperature of model was set to 200 °C and a temperature boundary with 0 °C was applied on the bottom surface.

The obtained temperature results are shown in Fig. 13. For both NTD and TD conditions, several small and major cracks propagate from the bottom to the top surfaces. After around 250 s, most cracks stop propagating. For the TD condition, as the thermal conductivity decreases and the specific heat capacity increases with elevated temperature, the heat conduction process is slower than that with the NTD condition. Cracks patterns are shown in Fig. 14. Many

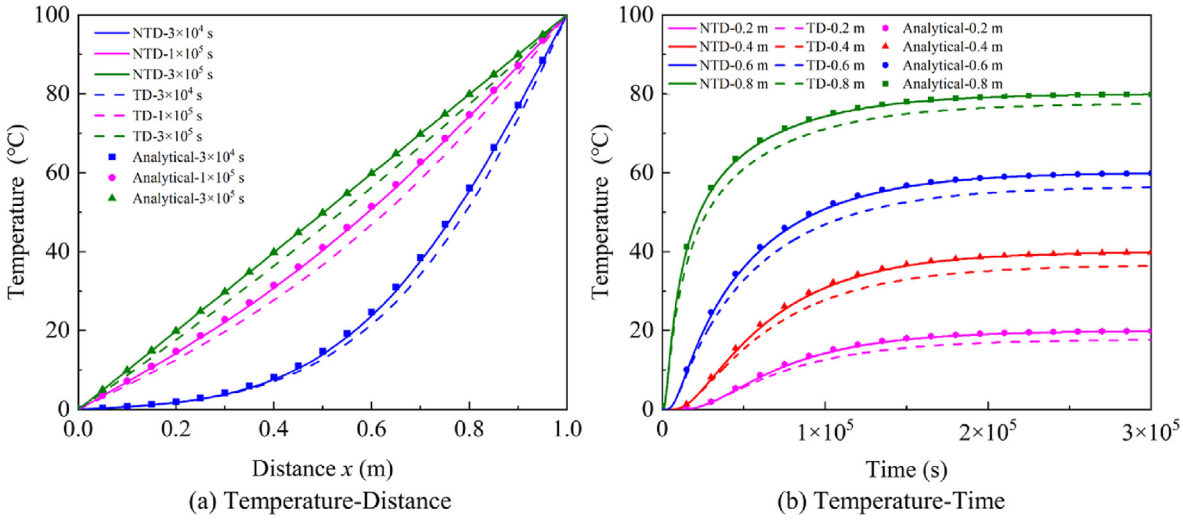

Fig. 5. Spato-temporal distribution of temperature.

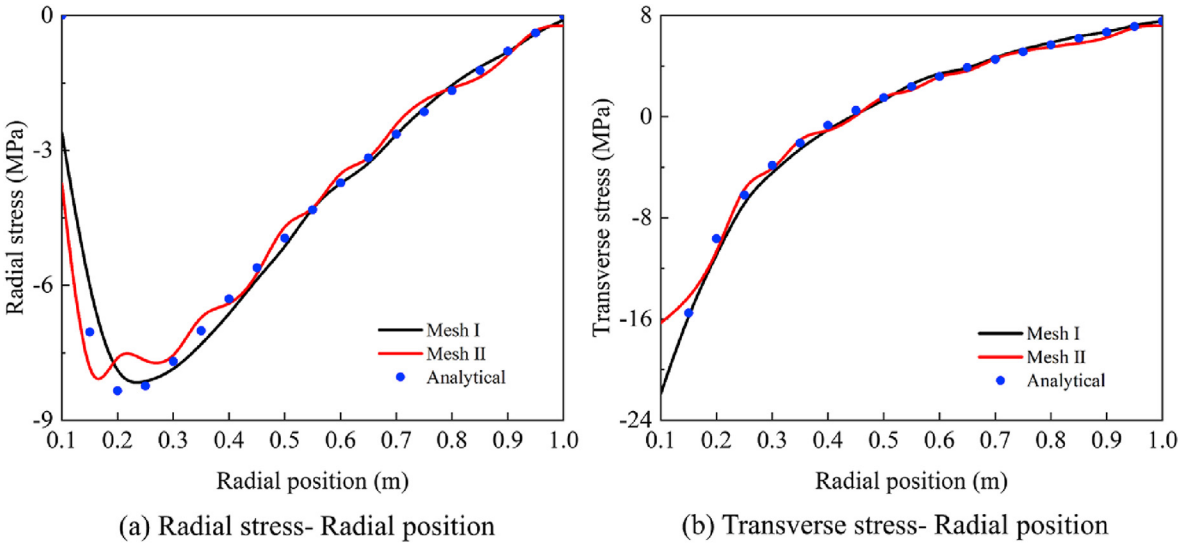

Fig. 7. Distribution of thermal stress of NTD model.

micro-cracks appear in the regions close to the bottom surface while several major cracks appear in the upper regions. These crack patterns agree with the results of Yan et al. (2022).

3.2. Thermal expansion mismatch test

The thermal expansion properties of different minerals are varied, resulting in non-uniform deformation and so-called thermal mismatch stress (TMS) (Yan and Zheng, 2017). The test for the TMS is shown in Fig. 15 with parameters for the two materials listed in Table 2 (Yan and Zheng, 2017; Shou and Zhou, 2020). The initial temperature of the whole model was set to 0 °C. The whole model experiences uniform temperature rising from 0 °C to 300 °C within 300 s when the thermal expansion coefficient of the embedded medium is larger than that of the matrix. When the temperature rises, the matrix structure experiences tension and the embedded medium experiences compression.

Fig. 16 shows the evolution of the maximum principal stress considering the TD and NTD conditions. For the matrix structure, when the tensile stress exceeds the strength of extension, the cracks will appear and the stress will be released (Fig. 16a and e). Crack evolutions are shown in Fig. 17. Cracks first appear at the

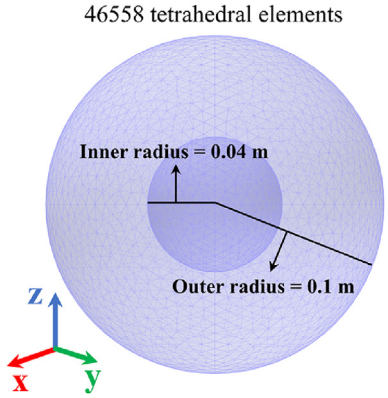

Fig. 9. Thermal cracking of a hollow sphere model.

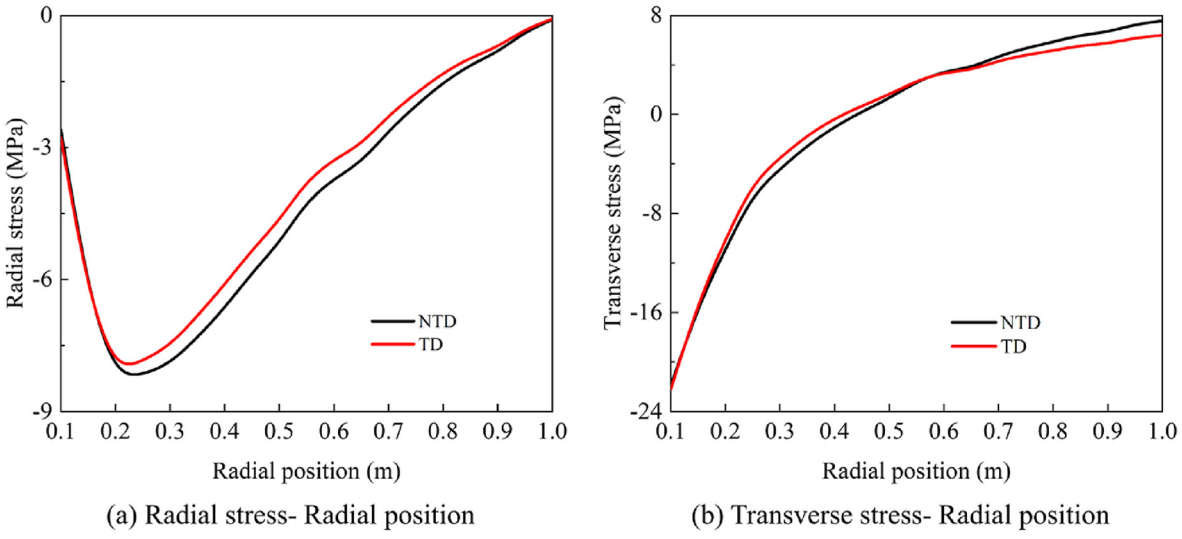

Fig. 8. Comparison of thermal stresses between NTD and TD models of mesh I.

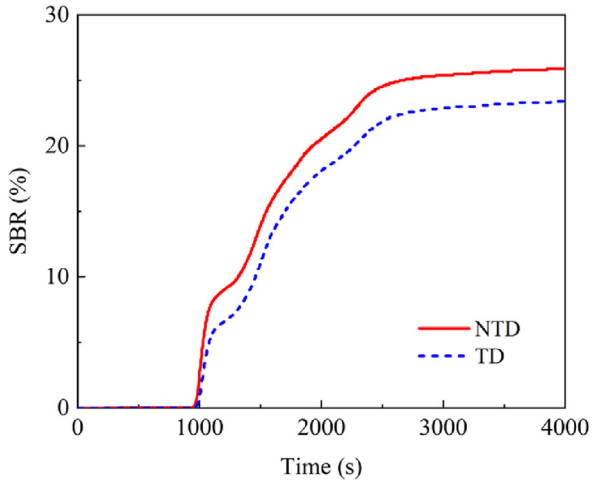

Fig. 10. The numerically-obtained SBR.

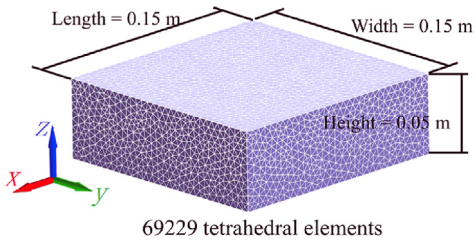

Fig. 12. Thermal shock of a heated block model.

interface between the matrix and the embedded medium (see Fig. 17a and e). Then, several major cracks continue to propagate radially. The final cracking patterns generally agree with that of Shou and Zhou (2020). For the TD condition, when the tensile strength decreases with increasing temperature, more cracks emerge and the SBR is higher (Fig. 18a). The maximum spring normal forces are shown in Fig. 18b, indicating the springs in loading-breaking procedures continuously during heating.

3.3. Simulation of a geothermal injection well

Geothermal energy is recognized as a clean energy (Phuoc et al., 2018). The mining method is to inject low-temperature medium (water and supercritical carbon dioxide) into high-temperature rock layer through the injection well and extract the high-temperature medium fluid back from the production well to the ground plant for heating, as shown in Fig. 19a (Xu et al., 2022; Zhang et al., 2022).

The surrounding rocks of the geothermal injection well may experience cracks induced by in situ stress as well as thermal stress (Du et al., 2017). Such cracking can decrease the efficiency of geothermal exploitation. In this example, the surrounding rock was simplified into a hollow cylinder model with outer radius 0.6 m, inner radius 0.1 m, and height 0.3 m (Fig. 19b). The material is granite with the same parameters used in Section 2.4.3. Constrained displacement was specified in the inner surface of the model to simulate the supporting effect of the geothermal well. Different pressure levels (0 MPa, 5 MPa and 10 MPa) were considered on the other surfaces to simulate the in situ stress. The initial temperature is 250 °C. For boundary conditions, the temperature of inner surface is 20 °C and the temperature of outer surface is 250 °C.

As mentioned before, for granite, the specific heat capacity increases and the thermal conductivity decreases with elevating temperature. Hence, for the TD condition, the heat conduction is slower and the temperature gradient is higher than that of the NTD condition for the same time step, as illustrated in Fig. 20. Taking case with the in situ stress (5 MPa) as an example, the maximum principal stresses are shown in Fig. 21. After applying the relatively low boundary temperature, the inner regions shrink as the cold shock, resulting in high tensile stress. The regions with tensile stress expand with elapsed time, and then become smooth.

Fig. 22 shows the final cracking patterns considering different in situ stresses with the TD and NTD conditions. It can be found that higher in situ stresses constraint crack propagation. The cracking patterns with the TD and NTD conditions are generally similar. On the other hand, Fig. 23 shows the evolutions of the SBR, indicating the damage level of TD is lower than that of NTD with in situ stress while the damage level of TD is higher than that of NTD with high in

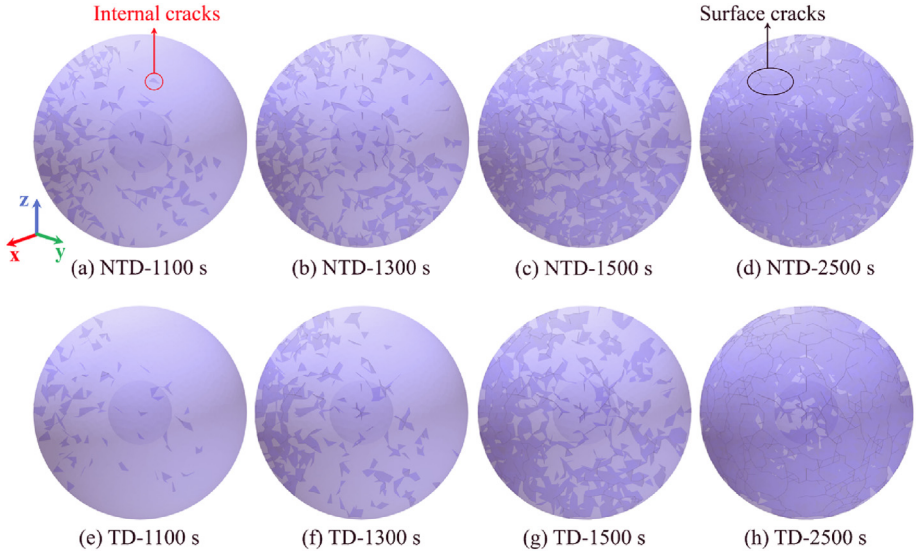

Fig. 11. Cracking patterns at different time steps.

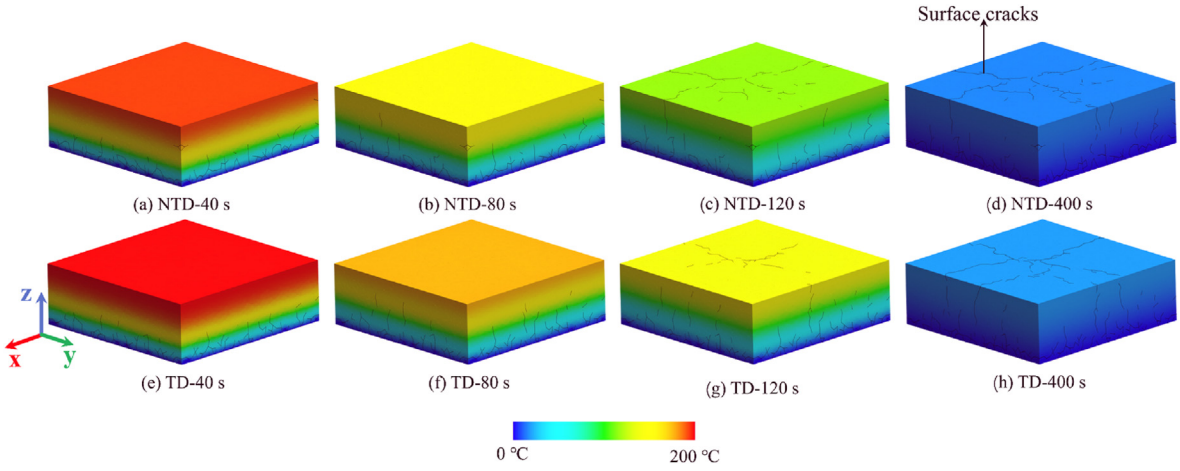

Fig. 13. Temperature evolution of NTD and TD models.

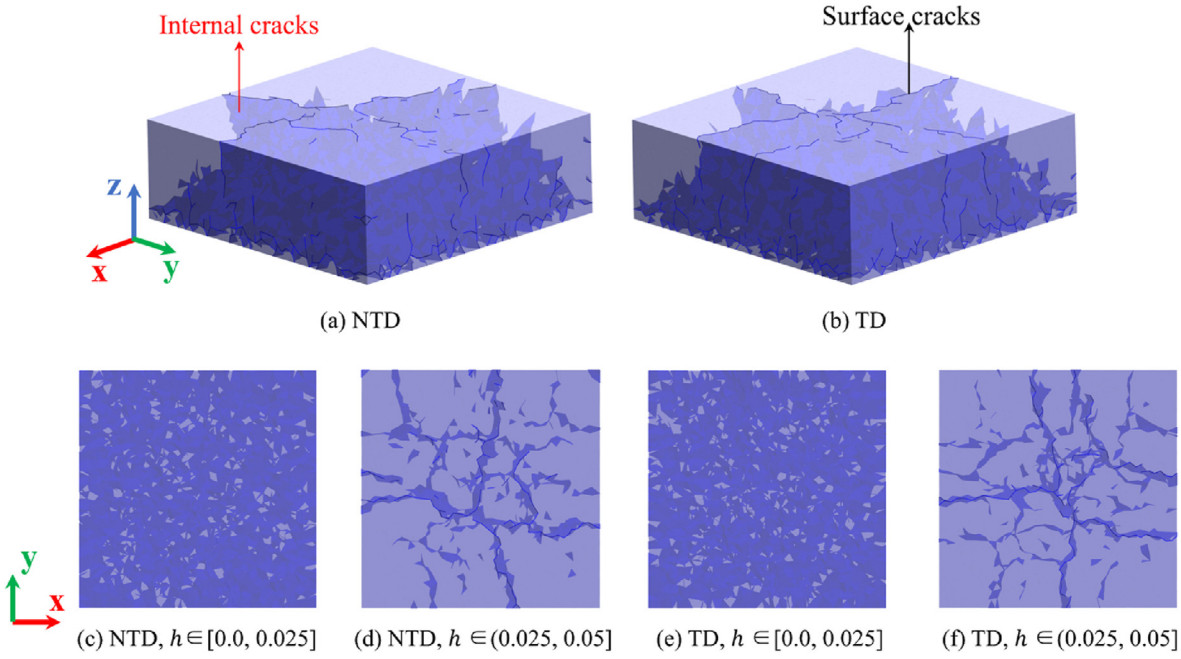

Fig. 14. Comparison of cracking patterns of NTD and TD models at 400 s (h: the distance to the bottom of model).

situ stress. This is because the elastic modulus decreases with increasing temperature in the TD conditions. At in situ stress of 10 MPa, the inner regions are stiffer in the TD condition than that in the NTD condition, rendering higher stresses and more cracks in the TD condition.

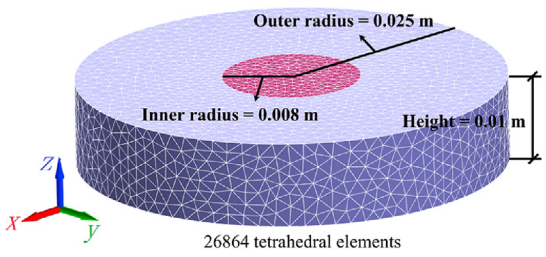

Fig. 15. Thermal expansion mismatch test model.

4. Discussion

Since the CDEM is an explicit iterative numerical method, a small time-step must be used to ensure the convergence, which also leads to the relatively low calculation speed, especially in the 3D case. A personal computer with Intel Core i7-11800H 2.30G Hz processor and 16 GB memory was used to obtain the numerical results in this paper. Fig. 24 shows the average time of each computation step for different models, where the unit CPU time is defined as the computing time over the number of block elements at each step. It can be found that the unit CPU time increases almost linearly with increasing block elements. Moreover, the unit CPU time of the 3D models takes about twice that of the 2D models. Therefore, it is still a challenge to improve the computational speed of CDEM in large-scale elements.

Table 2
Material parameters.

Parameters	Units	Matrix	Embedded medium
Density, ρ	kg/m^3	2700	2700
Young's modulus, E_0	GPa	20	20
Poisson's ratio, ν_0	–	0.2	0.3
Tensile strength, $f_{t,0}$	MPa	10	20
Cohesion, c_0	MPa	20	20
Friction angle, ϕ	°	30	30
Thermal conductivity, k_0	W/(m °C)	1.2	1.2
Specific heat, $c_{p,0}$	J/(kg °C)	900	900
Thermal expansion coefficient, α_T	°C^{-1}	1.5×10^{-5}	1×10^{-5}

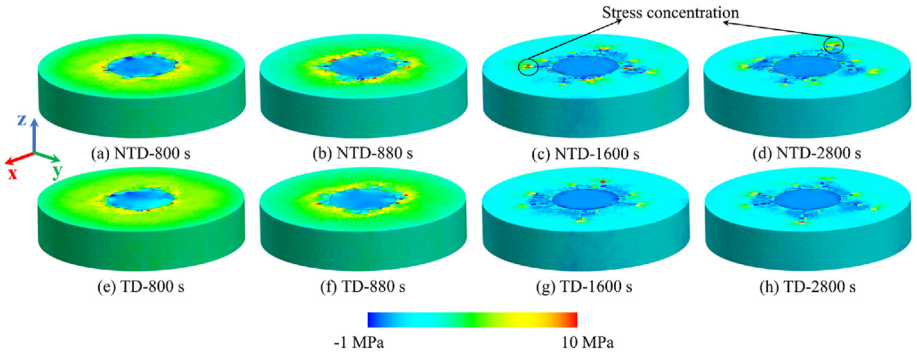

Fig. 16. Maximum principal stress evolution of NTD and TD models caused by TMS.

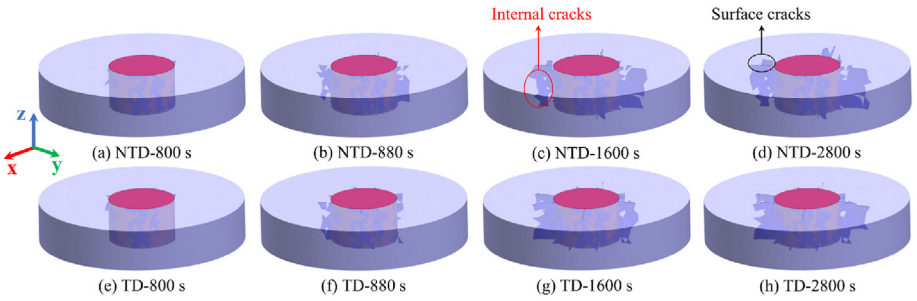

Fig. 17. Cracking patterns of NTD and TD models caused by TMS.

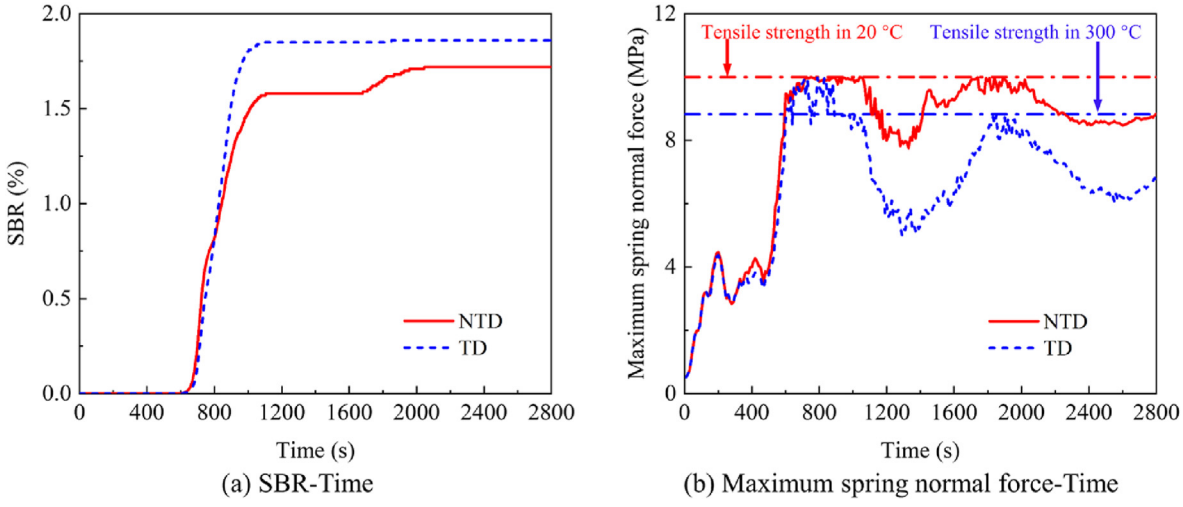

Fig. 18. SBR and maximum spring normal force of NTD and TD models.

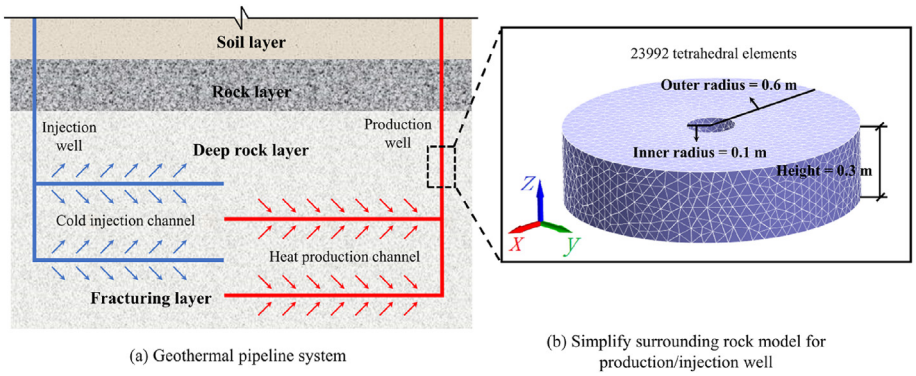

Fig. 19. Geothermal system and the simplified model.

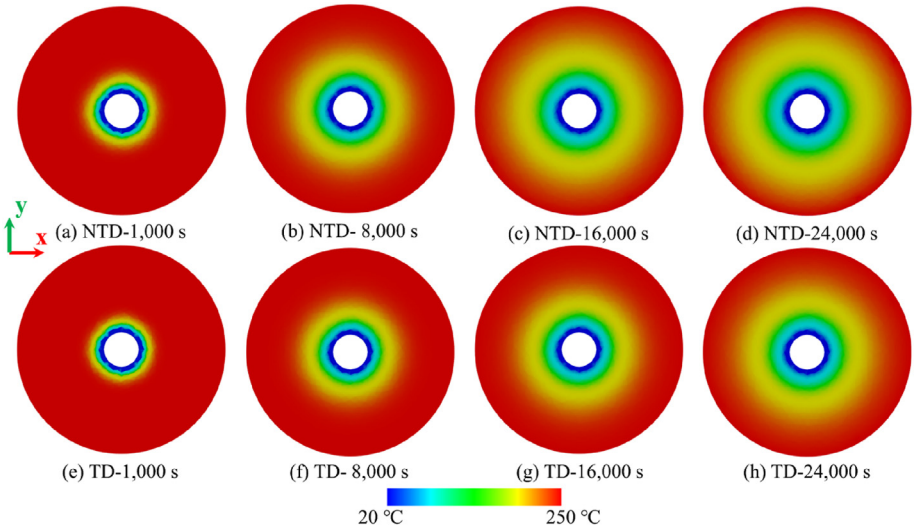

Fig. 20. Evolution of the temperature of NTD and TD models with 5 MPa ground pressure.

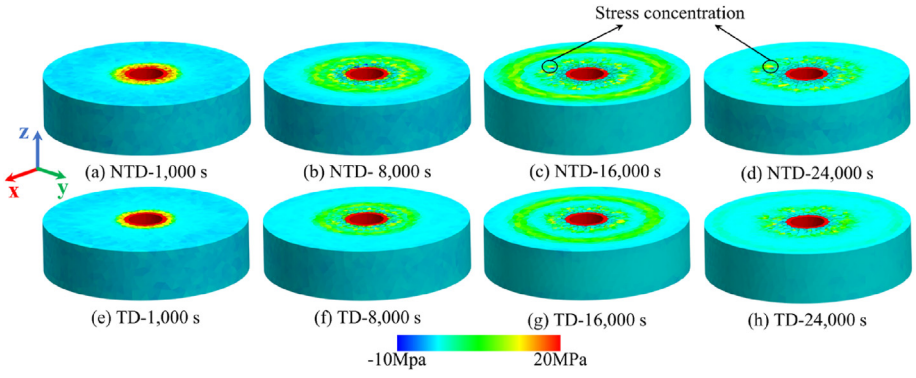

Fig. 21. Evolution of the maximum principal stress of NTD and TD models with 5 MPa ground pressure.

5. Conclusion

In this paper, a 3D numerical model for simulating thermal cracking of rocks was proposed. By using simplex integration, the thermal energy in tetrahedral element was calculated. Using an updating procedure, the temperature dependent material properties were taken into account in the framework of CDEM, as an explicit iterative numerical method coupling finite and discrete elements. Several benchmark tests and numerical examples were considered. By comparing the obtained results with analytical and numerical solutions, the reliability and robustness of the numerical model were verified.

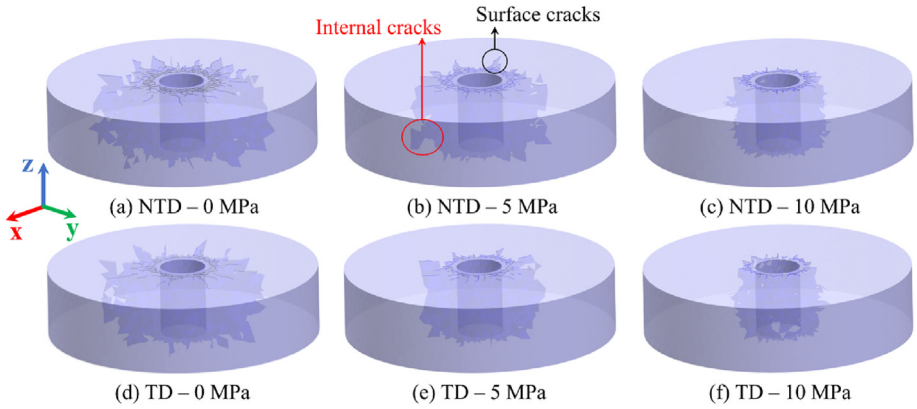

Fig. 22. Cracking patterns with different ground pressures.

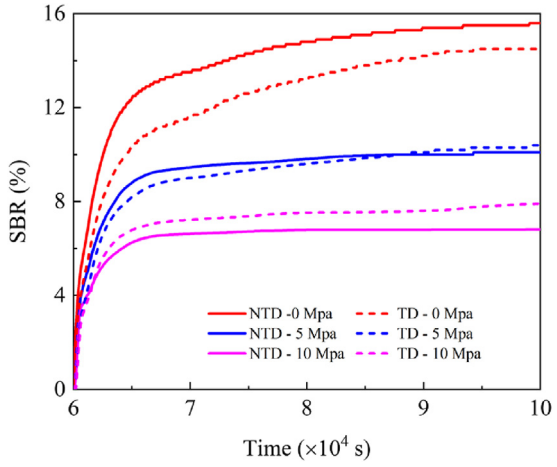

Fig. 23. Comparison of SBR of injection well with different ground pressures.

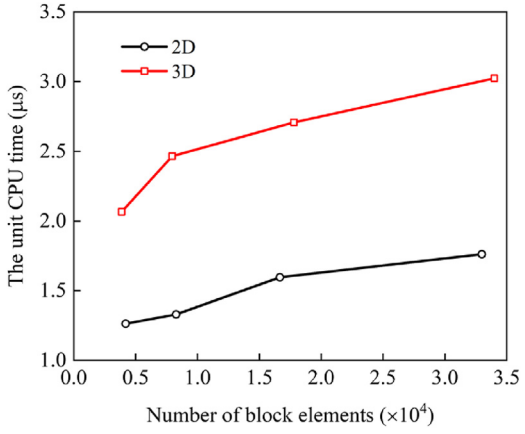

Fig. 24. The unit CPU time of the examples with different number of elements.

Declaration of competing interest

The authors declare that they have no known competing financial interests or personal relationships that could have appeared to influence the work reported in this paper.

Acknowledgments

The authors gratefully acknowledge the financial support from the Natural Science Foundation of Hebei Province (Grant No. E2020050012), the National Natural Science Foundation of China (NSFC) (Grant No. 52178324), and the National Key Research and Development Project of China, the Ministry of Science and Technology of China (Grant No. 2018YFC1505504).

Appendix A. Supplementary data

Supplementary data to this article can be found online at https://doi.org/10.1016/j.jrmge.2023.02.017.

List of Symbols

Q_i	Non-conservative force of the system
L	Lagrange function
t	Node time
t_n	Present time step
Δt	Time increment
u_i	Nodal displacement
$\dot{u}_i$	Nodal velocity
$\boldsymbol{u}(t)$	Displacement vector of element nodes at time
$\dot{\boldsymbol{u}}(t)$	Velocity vector of element nodes at time
$\ddot{\boldsymbol{u}}(t)$	Acceleration vector of element nodes at time
$\boldsymbol{M}$	Concentrated mass matrices of element
$\boldsymbol{C}$	Damping matrices of element
$\boldsymbol{K}$	Stiffness matrices of element
$\boldsymbol{F}$	External force vector
$\boldsymbol{n}$	Outer normal vector of $\partial\Omega$
$\partial\Omega$	Boundary of element
$F_{\mathrm{n}}, F_{\tau 1}, F_{\tau 2}$	Normal and two tangential forces of the contact springs
$\Delta d_{\mathrm{n}}, \Delta d_{\tau 1}, \Delta d_{\tau 2}$	Normal and two tangential displacement increments of the contact springs
K_{n}, K_{τ}	Normal and tangential stiffness of the contact springs
A_{c}	Contact area of the springs
c_{t_n}	Cohesion of material at time t_n
f_{t,t_n}	Tensile strength of spring at time t_n
k_{t_n}	Thermal conductivity of material at time t_n
c_{p,t_n}	Specific heat capacity of material at time t_n
Q_n	Total heat flow of node
T	Temperature function
$\vec{i}, \vec{j}, \vec{k}$	Direction vectors
x, y, z	Components of spatial coordinate
ds	Surface integral of outer surface
q_i	Heat flux in element

N_i Shape function of elements
T_i Temperature of nodes
a_i, b_i, c_i, d_i Parameters of the shape function
$\overrightarrow{T_x}$, $\overrightarrow{T_y}$, $\overrightarrow{T_z}$ Components of the unit normal vectors of the temperature function along x, y, and z directions
E_0 Young's modulus
ν_0 Poisson's ratio
c_0 Cohesion
k_0 Thermal conductivity
$c_{p,0}$ Specific heat
$f_{t,0}$ Tensile strength
ρ Density of material
V Volume of element
ϕ Internal friction angle
α_T Thermal expansion coefficient
T_r Temperature at outside boundary
T_R Temperature at inside boundary
σ_r Radial stress
σ_θ Transverse stress

References

Azarafza, M., Asghari-Kaljahi, E., Akgün, H., 2017. Numerical modeling of discontinuous rock slopes utilizing the 3DDGM (three-dimensional discontinuity geometrical modeling) method. Bull. Eng. Geol. Environ. 76, 989–1007.

Azarafza, M., Akgun, H., Asghari Kaljahi, E., 2018. Stochastic geometry model of rock mass fracture network in tunnels. Q. J. Eng. Geol. Hydrogeol. 51, 379–386.

Boon, C.W., Houlsby, G.T., Utili, S., 2012. A new algorithm for contact detection between convex polygonal and polyhedral particles in the discrete element method. Comput. Geotech. 44, 73–82.

Chadaram, S., Yadav, S.K., 2021. Three-dimensional thermal fracture analysis of piezoelectric material by extended finite element methods. Eng. Fract. Mech. 256, 107981.

Chen, S., Yang, C., Wang, G., 2017. Evolution of thermal damage and permeability of Beishan granite. Appl. Therm. Eng. 110, 1533–1542.

Chen, Y., Wang, S., Guo, C., Lin, C., Zhao, C., 2022. Analyses of non-aqueous reactive polymer insulation layer in high geothermal tunnel. J. Rock Mech. Geotech. Eng. 15 (1), 169–178.

Du, C., Cao, P., Chen, Y., Liu, J., Zhao, Y., Liu, J., 2017. Study on the stability and deformation of the roadway subjected to high in-situ stresses. Geotech. Geol. Eng. 35, 1615–1628.

Fan, L.F., Wu, Z.J., Wan, Z., Gao, J.W., 2017. Experimental investigation of thermal effects on dynamic behavior of granite. Appl. Therm. Eng. 125, 94–103.

Feng, C., Li, S., Liu, X., Zhang, Y., 2014. A semi-spring and semi-edge combined contact model in CDEM and its application to analysis of Jiweishan landslide. J. Rock Mech. Geotech. Eng. 6 (1), 26–35.

Huang, G., Tong, C., Zhang, S., Chen, X., 2022. A thermo-solid coupling model for disk discontinuous deformation analysis to simulate heating and stirring particles in rotary drums. Powder Technol. 402, 117326.

Jiang, Y., Zhu, Z., Yu, L., Zhou, L., Zhang, R., Ma, L., 2022. Investigation of the fracture characteristics of granite and green sandstone under different thermal treatments. Theor. Appl. Fract. Mech. 118, 103217.

Jiao, Y.Y., Zhang, X.L., Zhang, H.Q., Li, H.B., Yang, S.Q., Li, J.C., 2015. A coupled thermo-mechanical discontinuum model for simulating rock cracking induced by temperature stresses. Comput. Geotech. 67, 142–149.

Ju, Y., Liu, P., Chen, J., Yang, Y., Ranjith, P.G., 2016. CDEM-based analysis of the 3D initiation and propagation of hydrofracturing cracks in heterogeneous glutenites. J. Nat. Gas Sci. Eng. 35, 614–623.

Junique, T., Vázquez, P., Géraud, Y., Thomachot-Schneider, C., Sidibé, H., 2021. Microstructural evolution of granitic stones exposed to different thermal regimes analysed by infrared thermography. Eng. Geol. 286, 106057.

Lee, J.O., Choi, H., Kim, G.Y., 2017. Numerical simulation studies on predicting the peak temperature in the buffer of an HLW repository. Int. J. Heat Mass Tran. 115, 192–204.

Li, L., Feng, C., 2016. A numerical simulation method of heat conduction process in discontinuous medium. Mech. Eng. 33, 25–31.

Li, D., Ma, J., Wan, Q., Zhu, Q., Han, Z., 2021a. Effect of thermal treatment on the fracture toughness and subcritical crack growth of granite in double-torsion test. Eng. Fract. Mech. 253, 107903.

Li, T., Tang, C.A., Rutqvist, J., Hu, M., 2021b. TOUGH-RFPA: coupled thermal-hydraulic-mechanical Rock Failure Process Analysis with application to deep geothermal wells. Int. J. Rock Mech. Min. Sci. 142, 104726.

Li, X., Liu, J., Gong, W., Xu, Y., Bowa, V.M., 2022. A discrete fracture network based modeling scheme for analyzing the stability of highly fractured rock slope. Comput. Geotech. 141, 104558.

Lin, S., Xie, Z., 2020. A new recursive formula for integration of polynomial over simplex. Appl. Math. Comput. 376, 125140.

Liu, X., Liu, Q., Liu, B., Kang, Y., He, J., 2019. Numerical manifold method for thermal–hydraulic coupling in fractured enhance geothermal system. Eng. Anal. Bound. Elem. 101, 67–75.

Luo, X., Ma, Q., Yu, Q., Wang, X., Liu, Y., Wu, G., 2022. Field investigation on moisture, heat and deformation behaviors and their coupling effects of expressway in warm permafrost regions. Int. J. Heat Mass Tran. 191, 122858.

Mao, R., Mao, X., Zhang, L., Liu, R., 2015. Effect of loading rates on the characteristics of thermal damage for mudstone under different temperatures. Int. J. Min. Sci. Technol. 25, 797–801.

Mu, L., Zhang, Y., 2020. Cracking elements method with 6-node triangular element. Finite Elem. Anal. Des. 177, 103421.

Peng, K., Lv, H., Yan, F., Zou, Q., Song, X., Liu, Z., 2020a. Effects of temperature on mechanical properties of granite under different fracture modes. Eng. Fract. Mech. 226, 106838.

Peng, H., Zhao, Z., Chen, W., Chen, Y., Fang, J., Li, B., 2020b. Thermal effect on permeability in a single granite fracture: experiment and theoretical model. Int. J. Rock Mech. Min. Sci. 131, 104358.

Phuoc, T.X., Massoudi, M., Wang, P., Mckoy, M.L., 2018. Exergy of air, CO_2, and H_2O for use as geothermal fluids. Int. J. Heat Mass Tran. 126, 448–456.

Rabczuk, T., Belytschko, T., 2004. Cracking particles: a simplified meshfree method for arbitrary evolving cracks. Int. J. Numer. Methods Eng. 61 (13), 2316–2343.

Rabczuk, T., Belytschko, T., 2005. Adaptivity for structured meshfree particle methods in 2D and 3D. Int. J. Numer. Methods Eng. 63, 1559–1582.

Rabczuk, T., Belytschko, T., 2007. A three-dimensional large deformation meshfree method for arbitrary evolving cracks. Comput. Methods Appl. Mech. Eng. 196, 2777–2799.

Rabczuk, T., Bordas, S., Zi, G., 2007. A three-dimensional meshfree method for continuous multiple-crack initiation, propagation and junction in statics and dynamics. Comput. Mech. 40, 473–495.

Rabczuk, T., Zi, G., 2007. A meshfree method based on the local partition of unity for cohesive cracks. Comput. Mech. 39, 743–760.

Rao, S.S., 2018. Overview of finite element method. In: The Finite Element Method in Engineering, sixth ed. Butterworth-Heinemann, Woburn, MA, USA.

Rasmussen, L.L., 2020. UnBlocksgen: a Python library for 3D rock mass generation and analysis. Software 12, 100577.

Ren, H., Zhuang, X., Cai, Y., Rabczuk, T., 2016. Dual-horizon peridynamics. Int. J. Numer. Methods Eng. 108, 1451–1476.

Ren, H., Zhuang, X., Rabczuk, T., 2017. Dual-horizon peridynamics: a stable solution to varying horizons. Comput. Methods Appl. Mech. Eng. 318, 762–782.

Shang, J., Zhao, Z., Hu, J., Handley, K., 2018. 3D particle-based DEM investigation into the shear behaviour of incipient rock joints with various geometries of rock bridges. Rock Mech. Rock Eng. 51, 3563–3584.

Shou, Y., Zhou, X., 2020. A coupled thermomechanical nonordinary state-based peridynamics for thermally induced cracking of rocks. Fatig. Fract. Eng. Mater. Struct. 43 (2), 371–386.

Tao, S., Tang, X., Rutqvist, J., Hu, M., Liu, Q., 2020. Simulating three dimensional thermal cracking with TOUGH-FEMM. Comput. Geotech. 124, 103654.

Wang, F., Konietzky, H., 2019. Thermo-mechanical properties of granite at elevated temperatures and numerical simulation of thermal cracking. Rock Mech. Rock Eng. 52, 3737–3755.

Wang, F., Konietzky, H., 2022. Thermal cracking in granite during a heating–cooling cycle up to 1000 °C: laboratory testing and real-time simulation. Rock Mech. Rock Eng. 55, 1411–1428.

Wang, F., Konietzky, H., Frühwirt, T., Dai, Y., 2020. Laboratory testing and numerical simulation of properties and thermal-induced cracking of Eibenstock granite at elevated temperatures. Acta Geotech 15, 2259–2275.

Wang, F., Konietzky, H., Herbst, M., 2019a. Influence of heterogeneity on thermo-mechanical behaviour of rocks. Comput. Geotech. 116, 103184.

Wang, Y., Zhou, X., Kou, M., 2019b. An improved coupled thermo-mechanic bond-based peridynamic model for cracking behaviors in brittle solids subjected to thermal shocks. Eur. J. Mech. A Solids 73, 282–305.

Wang, G., Song, X., Song, G., Shi, Y., Yu, C., Xu, F., Ji, J., Song, Z., 2021. Analyzes of thermal characteristics of a hydrothermal coaxial closed-loop geothermal system in a horizontal well. Int. J. Heat Mass Tran. 180, 121755.

Wang, H., Yu, A., Feng, C., Ling, X., Chen, G., Gu, M., Zhu, X., 2022. An Efficient CDEM-based method to calculate full time-space natural fragment field of shell-bearing explosives. Int. J. Impact Eng. 161, 104099.

Wanne, T.S., Young, R.P., 2008. Bonded-particle modeling of thermally fractured granite. Int. J. Rock Mech. Min. Sci. 45, 789–799.

Wu, Y., Yin, T., Tan, X., Zhuang, D., 2021. Determination of the mixed mode I/II fracture characteristics of heat-treated granite specimens based on the extended finite element method. Eng. Fract. Mech. 252, 107818.

Wu, Z., Zhou, Y., Fan, L., 2019. A fracture aperture dependent thermal-cohesive coupled model for modelling thermal conduction in fractured rock mass. Comput. Geotech. 114, 103108.

Xia, M., 2015. Thermo-mechanical coupled particle model for rock. T. Nonferr. Metal. Soc. 25, 2367–2379.
Xu, D., Wu, A., Lu, B., Wang, B., Jiang, Y., Li, C., Liu, X., 2019. High-order discontinuous deformation analysis method for simulation of temperature field and thermal stress. Chin. J. Rock Mech. Eng. 38, 3595–3602 (in Chinese).
Xu, Y., Li, Z., Chen, Y., Jia, M., Zhang, M., Li, R., 2022. Synergetic mining of geothermal energy in deep mines: an innovative method for heat hazard control. Appl. Therm. Eng. 210, 118398.
Yan, C., Wang, X., Huang, D., Wang, G., 2021. A new 3D continuous-discontinuous heat conduction model and coupled thermomechanical model for simulating the thermal cracking of brittle materials. Int. J. Solid Struct. 229, 111123.
Yan, C., Wei, D., Wang, G., 2022. Three-dimensional finite discrete element-based contact heat transfer model considering thermal cracking in continuous–discontinuous media. Comput. Methods Appl. Mech. Eng. 388, 114228.
Yan, C., Zheng, H., 2017. A coupled thermo-mechanical model based on the combined finite-discrete element method for simulating thermal cracking of rock. Int. J. Rock Mech. Min. Sci. 91, 170–178.
Yang, J., Cheng, Y., Han, S., Yan, C., Xue, M., Ding, J., Chen, F., 2022. Research on the characteristics of crack propagation at high temperatures based on digital image correlation technology. Eng. Fract. Mech. 263, 108295.
Yu, H., Chen, X., Sun, Y., 2020. A generalized bond-based peridynamic model for quasi-brittle materials enriched with bond tension–rotation–shear coupling effects. Comput. Methods Appl. Mech. Eng. 372, 113405.
Yu, H., Sun, Y., 2021. Bridging the gap between local and nonlocal numerical methods—a unified variational framework for non-ordinary state-based peridynamics. Comput. Methods Appl. Mech. Eng. 384, 113962.
Yuan, J., Jiang, R., Cui, Y., Xu, J., Wang, Q., Zhang, W., 2019. The numerical simulation of thermal recovery considering rock deformation in shale gas reservoir. Int. J. Heat Mass Tran. 138, 719–728.
Zeng, Q., Yao, J., Shao, J., 2020. An extended finite element solution for hydraulic fracturing with thermo-hydro-elastic–plastic coupling. Comput. Methods Appl. Mech. Eng. 364, 112967.
Zhang, H.H., Liu, S.M., Han, S.Y., Fan, L.F., 2018. Modeling of 2D cracked FGMs under thermo-mechanical loadings with the numerical manifold method. Int. J. Mech. Sci. 148, 103–117.
Zhang, H.H., Ma, G.W., Ren, F., 2014. Implementation of the numerical manifold method for thermo-mechanical fracture of planar solids. Eng. Anal. Bound. Elem. 44, 45–54.
Zhang, J., Zhao, M., Wang, G., Ma, P., 2022. Evaluation of heat extraction performance of multi-well injection enhanced geothermal system. Appl. Therm. Eng. 201, 117808.
Zhang, W., Sun, Q., Hao, S., Geng, J., Lv, C., 2016. Experimental study on the variation of physical and mechanical properties of rock after high temperature treatment. Appl. Therm. Eng. 98, 1297–1304.
Zhang, W., Sun, Q., Zhu, S., Wang, B., 2017. Experimental study on mechanical and porous characteristics of limestone affected by high temperature. Appl. Therm. Eng. 110, 356–362.
Zhang, Y., 2001. Discussion about the thermal stress problem in DDA method. Chin. J. Rock Mech. Eng. 320, 277–278 (in Chinese).
Zhang, Y., Huang, J., Yuan, Y., Mang, H.A., 2021a. Cracking elements method with a dissipation-based arc-length approach. Finite Elem. Anal. Des. 195, 103573.
Zhang, Y., Yang, X., Wang, X., Zhuang, X., 2021b. A micropolar peridynamic model with non-uniform horizon for static damage of solids considering different nonlocal enhancements. Theor. Appl. Fract. Mech. 113, 102930.
Zhang, Y., Lackner, R., Zeiml, M., Mang, H.A., 2015. Strong discontinuity embedded approach with standard SOS formulation: element formulation, energy-based crack-tracking strategy, and validations. Comput. Methods Appl. Mech. Eng. 287, 335–366.
Zhang, Y., Mang, H.A., 2020. Global cracking elements: a novel tool for Galerkin-based approaches simulating quasi-brittle fracture. Int. J. Numer. Methods Eng. 121, 2462–2480.
Zhang, Y., Zhuang, X., 2018. Cracking elements: a self-propagating Strong Discontinuity embedded Approach for quasi-brittle fracture. Finite Elem. Anal. Des. 144, 84–100.
Zhang, Y., Zhuang, X., 2019. Cracking elements method for dynamic brittle fracture. Theor. Appl. Mech. 102, 1–9.
Zhou, Y., Ma, W., Tan, X., Chen, W., Yang, D., Su, Z., Zhang, X., Xu, F., 2021. Numerical simulation of fracture propagation in freezing rocks using the extended finite element method (XFEM). Int. J. Rock Mech. Min. Sci. 148, 104963.
Zhu, X., Feng, C., Cheng, P., Wang, X., Li, S., 2021. A novel three-dimensional hydraulic fracturing model based on continuum–discontinuum element method. Comput. Methods Appl. Mech. Eng. 383, 113887.

Yiming Zhang is currently a professor at Hebei University of Technology, China. He received his BSc and MSc degrees from Tongji University, China, and PhD from Vienna University of Technology, Austria. His research areas include computational mechanics, geotechnical engineering, disaster prevention, and mitigation engineering. He solved the stress locking problems of strong discontinuity embedded approach with the standard Statically Optimal Symmetric (SOS) formulation. He has received the Second Prize Award in Natural Sciences from Chinese Society for Rock Mechanics and Engineering (CSRME).